Supplementary Material

Geomorphic expression and slip rate of the Fairweather fault, southeast Alaska, and evidence for predecessors of the 1958 rupture

by Rob Witter[1], Adrian Bender[1], Kate Scharer[2], Chris DuRoss[3], Peter Haeussler[1], Richard Lease[1]

[1]*U.S. Geological Survey, Alaska Science Center, 4210 University Dr., Anchorage, AK, 99508, USA*
[2]*U.S. Geological Survey, Earthquake Science Center, 525 S. Wilson St., Pasadena, CA, 91106, USA*
[3]*U.S. Geological Survey, Geological Hazards Science Center, 1711 Illinois St., Golden, CO, 80401, USA*

These supplemental files includes ten figures, five tables, and GIS map files referenced in the article. The figures include legacy photographs and a 2018 satellite image that illustrate surface deformation and geomorphic features along the Fairweather fault (Figs. S1, S2, S5, and S6). Four figures present LaDiCaoz 2.1 analyses (Zielke et al., 2015; Haddon et al., 2016) used to measure offset of stream channels and moraines that cross the Fairweather fault trace (Figs. S3, S4, S7, and S8). Fig. S9 shows a supplemental photomosaic and log of trench A after scraping ~10 cm back into the north wall. Figs. S10 and S11 present photographs and field interpretations of two test pits across the Fairweather fault adjacent to trench A at the Tocher fan site. Table S1 lists the preferred, range, and quality of horizontal offsets of landforms at the Crillon fan and Finger Glacier sites measured using LaDiCaoz. Radiocarbon analyses using OxCal Sequence models (version 4.3, Bronk Ramsey [2009]), including results and code, are shown in Tables S2–S4. Finally, GIS shapefiles that include geomorphic lineaments, surficial geologic units, unit contacts, and active faults are included with a ReadMe in a zipped compressed file.

SUPPLEMENTAL REFERENCES

Page, R., 1969, Late Cenozoic movement on the Fairweather fault in southeastern Alaska: Geological Society of America Bulletin, v. 80, p. 1873–1878.

Salisbury, J.B., Haddad, D.E., Rockwell, T., Arrowsmith, J.R., Madugo, C., Zielke, O., and Scharer, K., 2015, Validation of meter-scale surface faulting offset measurements from high-resolution topographic data: Geosphere, v. 11, p. 1884–1901, doi: 10.1130/GES01197.1.

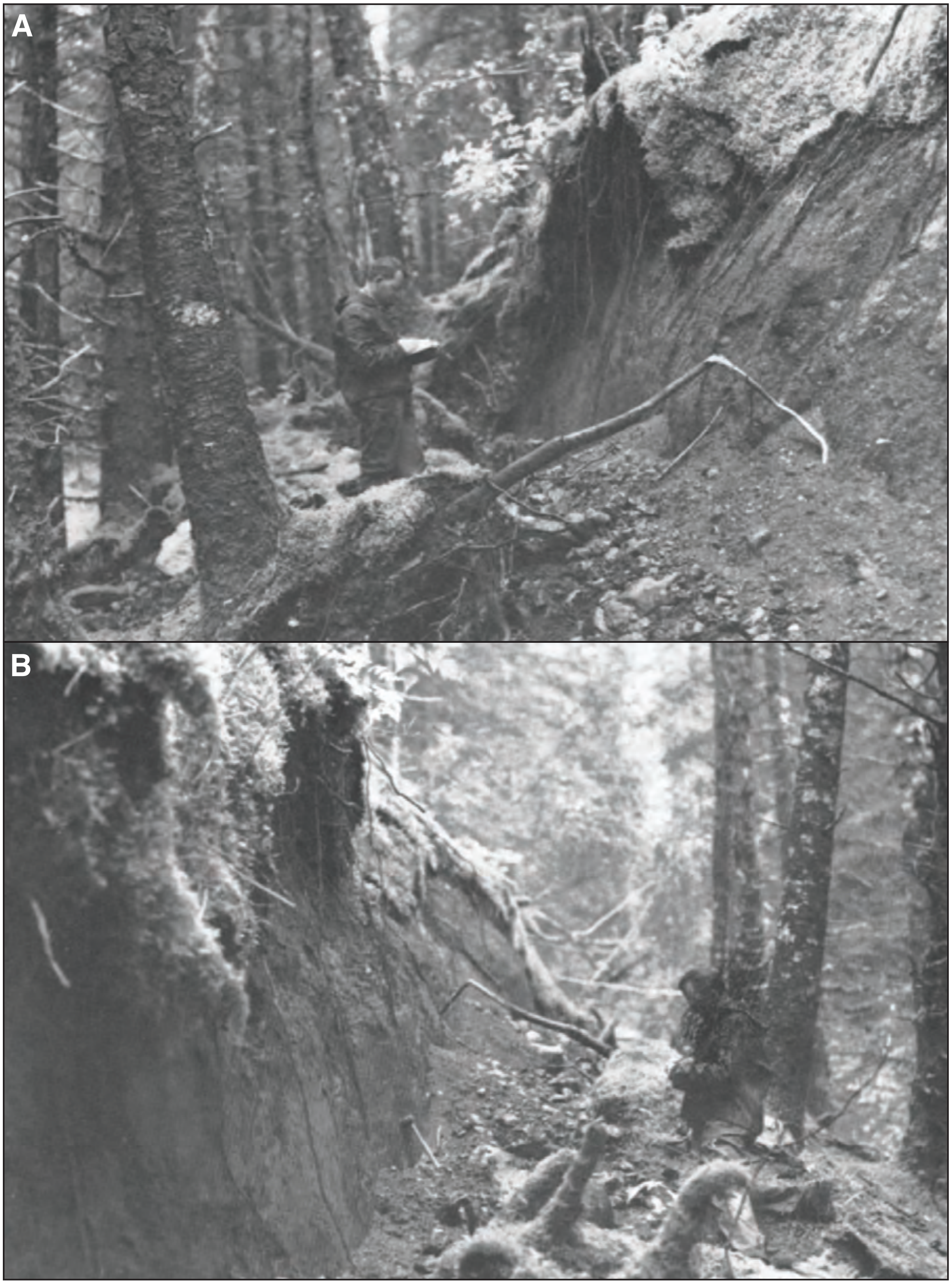

Figure S1. (A) Fault scarp described by Don Tocher (1960) at the Crillon fan site, view to the southeast. (B) Same fault scarp, view to the northwest. Both photographs taken on 2 September 1958 by D. Miller, USGS and previously published by Page (1969b).

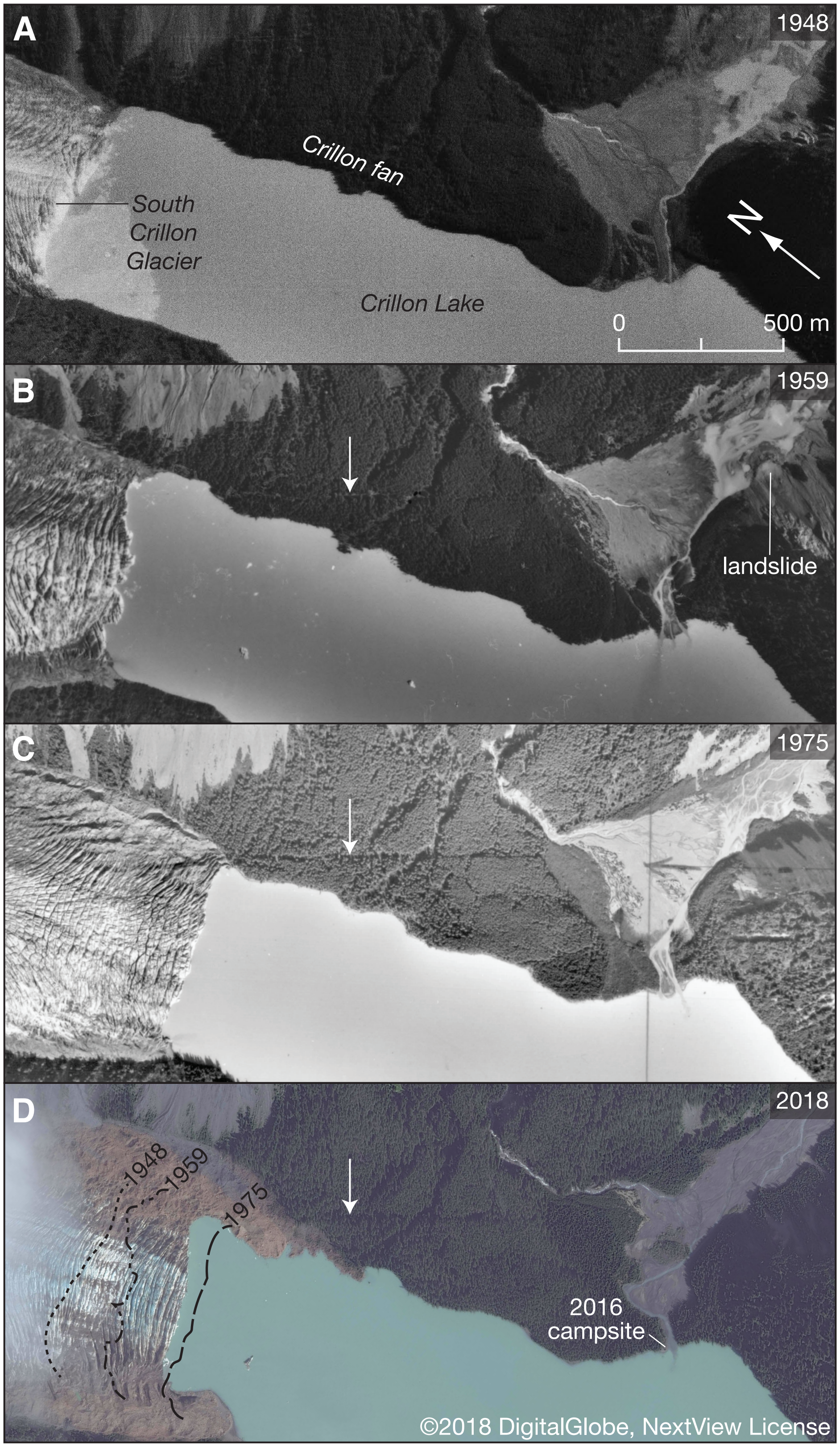

Figure S2. (A) Aerial photography taken in 1948 of the northeast end of Crillon Lake and the South Crillon glacier (USGS, Earth Resources Observation and Science Center, https://doi.org/10.5066/F7610XKM). (B) Same view taken in 1959 after the 1958 Fairweather earthquake (USGS, G. Plafker, unpublished data). White arrow marks cleft in forest where the 1958 surface fault rupture toppled trees. A landslide not present in 1948 is evident on the right of the 1959 photo. (C) Same view taken in 1975 (USGS, G. Plafker). (D) Satellite image of the same area in 2018 (©2018 DigitalGlobe, NextView License). Black dashed lines delineate advance of the ice terminus since 1948.

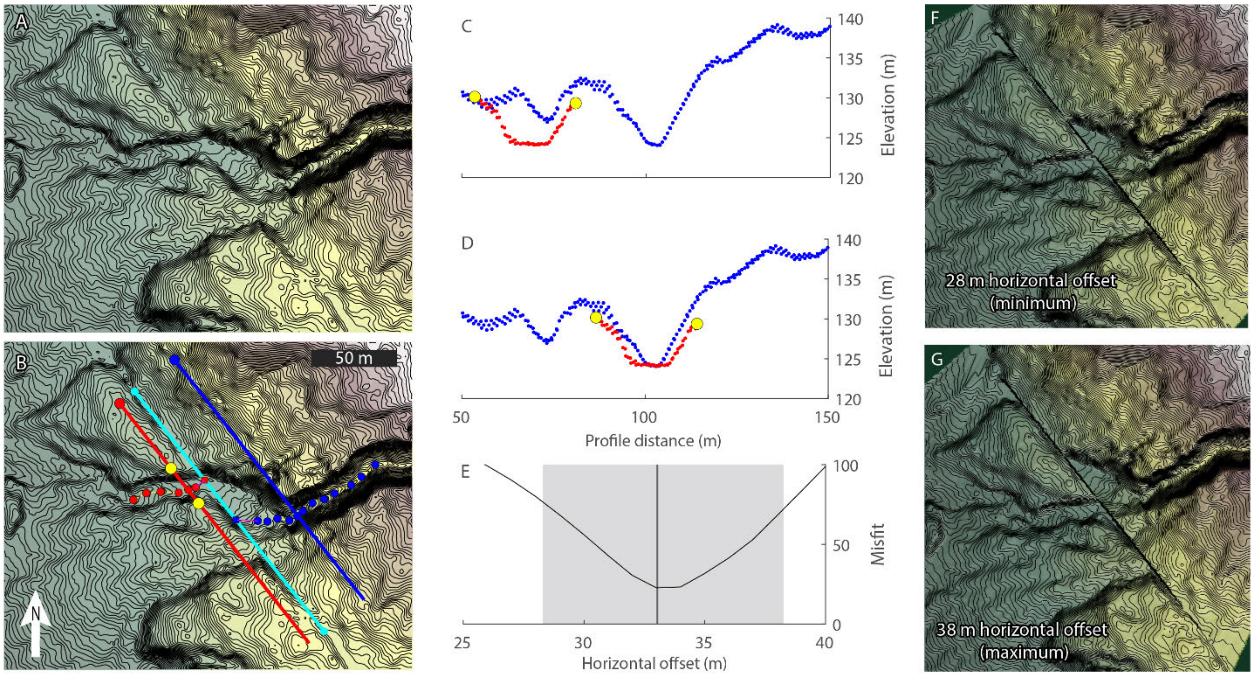

Figure S3. Central Crillon Lake channel offset across the primary Fairweather fault trace (Table S1) analyzed in LaDiCaoz 2.1 (Zielke et al., 2015; Haddon et al., 2016). A. Base lidar map, elevation contours on 0.5-meter intervals. B. Offset analysis setup: topographic profiles (red and blue lines) and traced thalweg (red and blue dots) across the primary Fairweather fault trace (cyan line). Yellow dots mark bounds on red channel topography fit to blue channel topography. C. *In-situ* topographic profiles; red dots represent beheaded channel cross-section selected (within yellow dots) for cross-correlation to channel within blue topographic profile, across the fault trace. D. Topographic profiles restored via cross-correlation: red channel cross-section back-slipped 33 meters to blue channel cross-section across the fault trace. E. Misfit curve for cross-correlation of red and blue crest cross sections; minimal misfit value marked by dark gray vertical bar represents best horizontal offset value from cross-correlation, light gray bar delineates visually determined offset range. F. Minimum horizontal offset (28 m) visually determined from back-slipping. G. Maximum horizontal offset (38 m) visually determined from back-slipping.

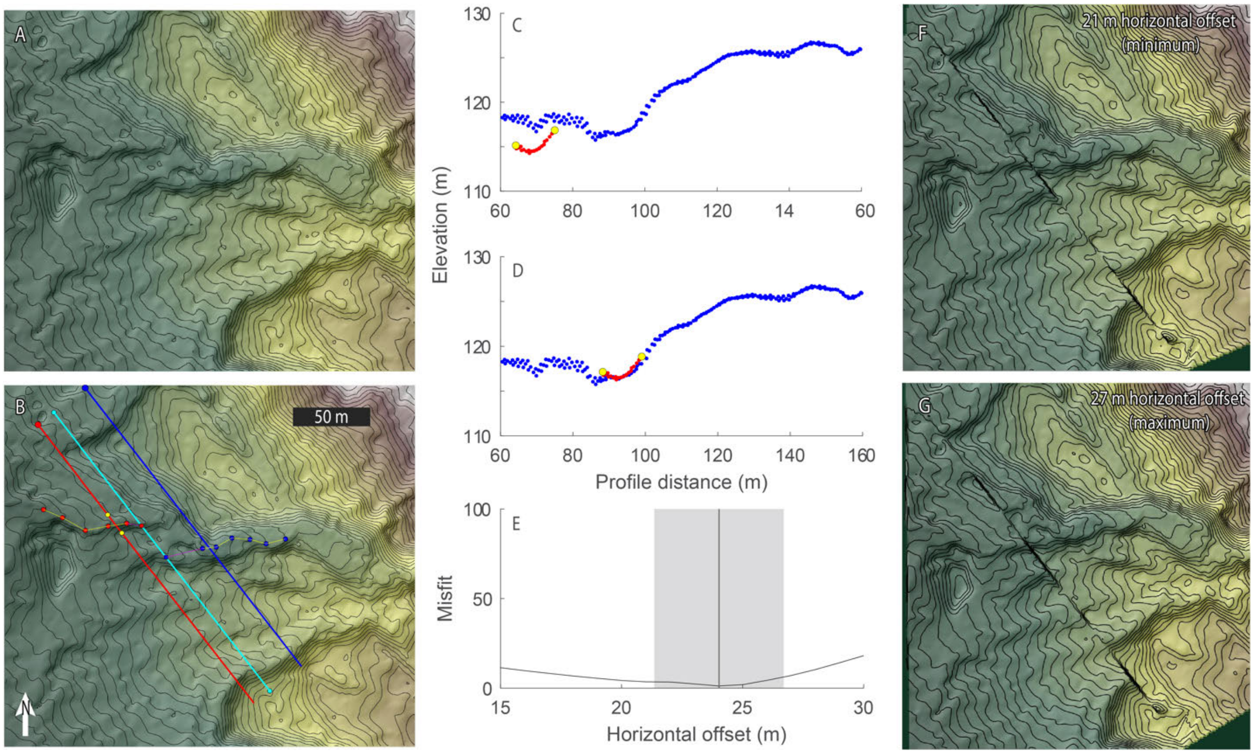

Figure S4. Central Crillon Lake channel offset across the secondary Fairweather fault trace (Table S1) analyzed in LaDiCaoz 2.1 (Zielke et al., 2015; Haddon et al., 2016). A. Base lidar map, elevation contours on 1-meter intervals. B. Offset analysis setup: topographic profiles (red and blue lines) and traced thalweg (red and blue dots) across the secondary Fairweather fault trace (cyan line). Yellow dots mark bounds on red channel topography fit to blue channel topography. C. In-situ topographic profiles; red dots represent beheaded channel cross section selected (within yellow dots) for cross correlation to channel within blue topographic profile, across the fault trace. D. Topographic profiles restored via cross correlation: red channel cross-section back-slipped 24 meters to blue channel cross-section across fault trace. Vertical shift of 2 m raises downstream thalweg elevations and may not be tectonic. E. Misfit curve for cross-correlation of red and blue crest cross sections; minimal misfit value marked by dark gray vertical bar represents best horizontal offset value from cross-correlation, light gray bar delineates visually determined offset range. F. Minimum horizontal offset (21 m) visually determined from back-slipping. G. Maximum horizontal offset (27 m) visually determined from back-slipping.

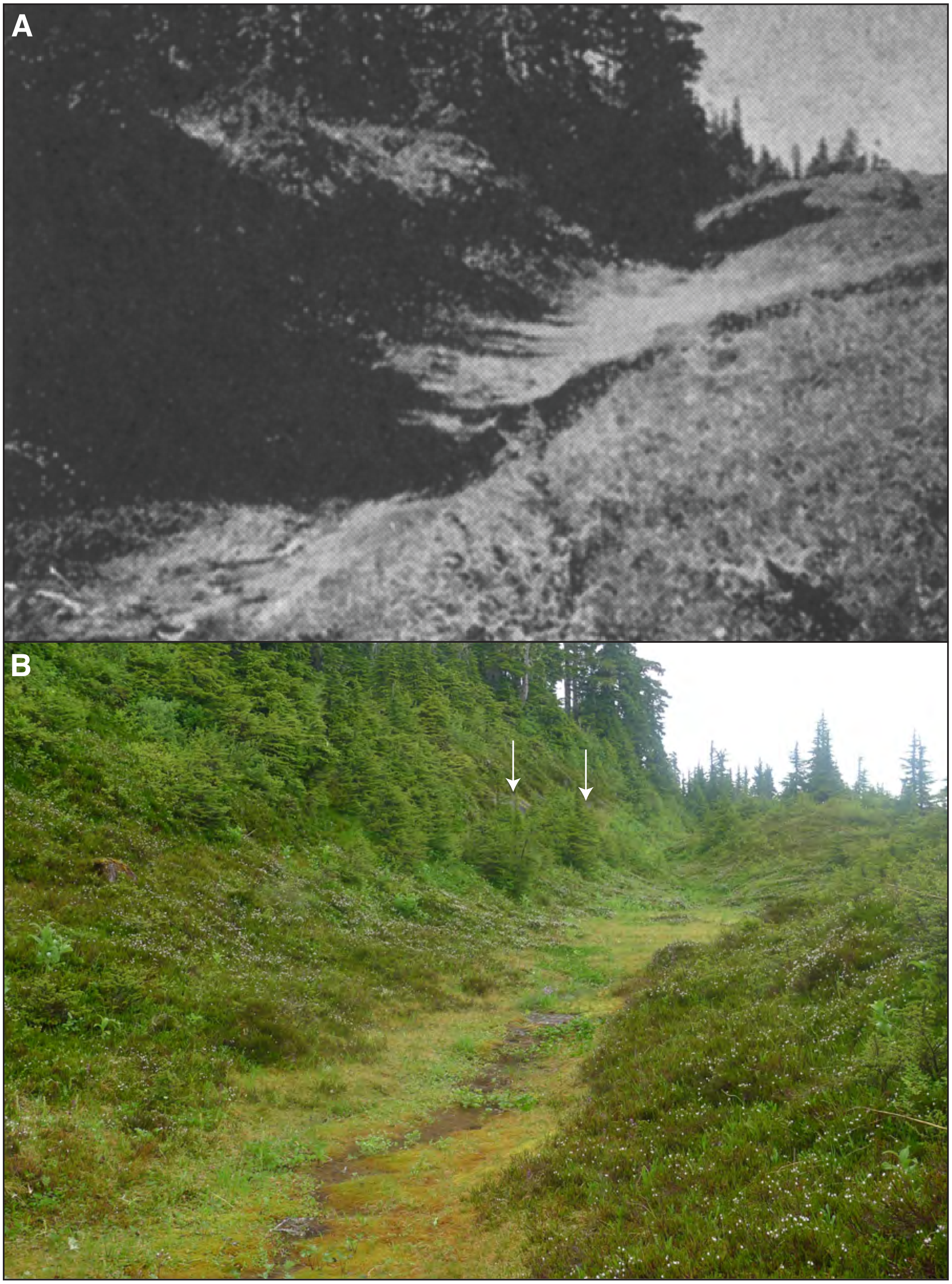

Figure S5. (A) Northeast flank of axial ridge near Tocher fan site; view to the northwest on 1 September 1959 (credit: D. Miller, USGS). Tocher (1960) published this photo with the caption, “The main rift active July 10, 1958 is marked by areas of light-colored, freshly exposed soil in the shadows, a few feet above the creek bottom.” (B) Same fault scarp, view to the northwest, taken on 26 June 2016 (credit: R. Witter, USGS). Arrows point to exposed colluvium along the scarp where the slope is steepest, possibly marking surface fault rupture in 1958.

Figure S6. Scanned image of 35 mm color slide taken by D. Miller during post-1958 earthquake surveys, view to northwest. Writing on the slide states, “Scarps formed during July 1958 quake, ridge SE of Fairweather fault near Crillon L.” We infer that the scarp in this image resulted from ridge-top spreading. The exact location is unknown, but the context of the photo places it along one of many uphill-facing scarps in bedrock northeast of the Tocher fan site.

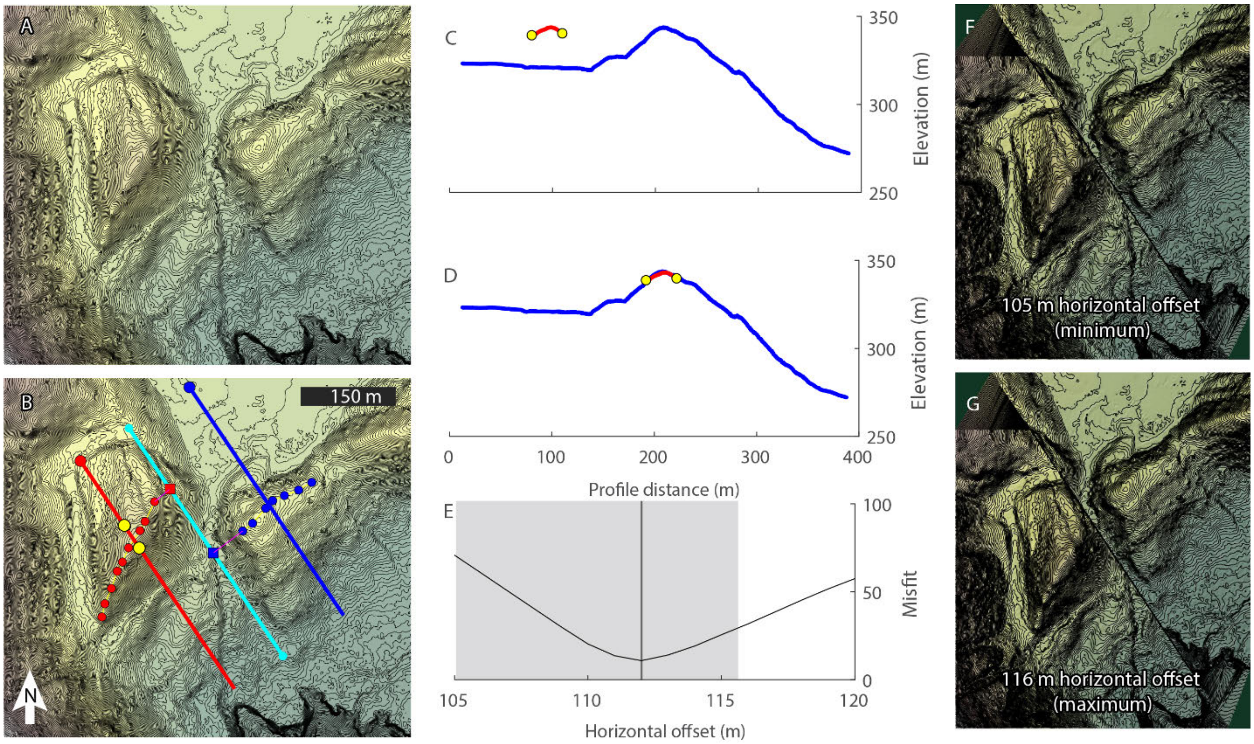

Figure S7. The highest Finger Glacier lateral moraine crest offset across the Fairweather fault zone (Table S1) analyzed in LaDiCaoz 2.1 (Zielke et al., 2015; Haddon et al., 2016). A. Base lidar map, elevation contours on 1-meter intervals. B. Offset analysis setup: topographic profiles (red and blue lines) and traced crest (red and blue dots) across the Fairweather fault zone (cyan line). Yellow dots mark bounds on red crest topography fit to blue crest topography. C. *In-situ* topographic profiles; red dots represent moraine crest cross-section selected (within yellow dots) for cross-correlation to crest along blue topographic profile, across the fault. D. Topographic profiles restored via cross-correlation: red crest cross-section back-slipped 112 meters to blue crest cross-section across fault. No vertical shift. E. Misfit curve for cross-correlation of red and blue crest cross sections; minimal misfit value marked by dark gray vertical bar represents best horizontal offset value from cross-correlation, light gray bar delineates visually determined offset range. F. Minimum horizontal offset (105 m) visually determined from back-slipping. G. Maximum horizontal offset (116 m) visually determined from back-slipping.

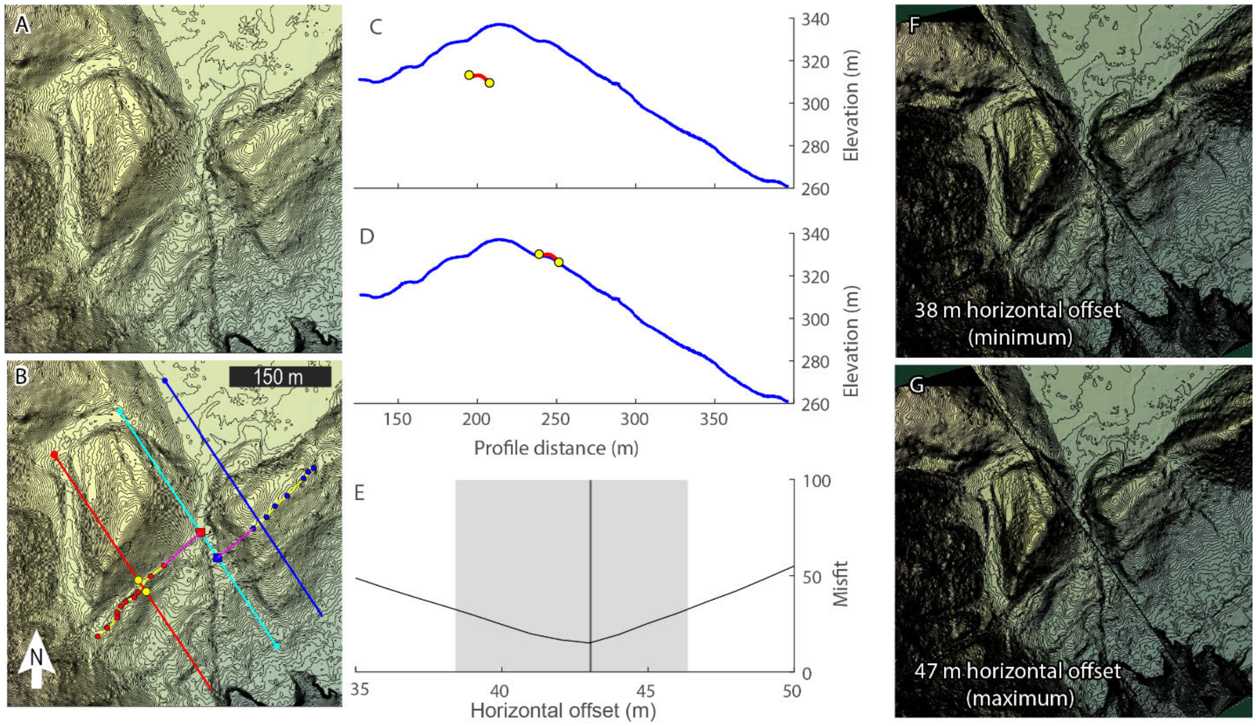

Figure S8. The Finger Glacier lateral moraine of Plafker and others (1978) offset across the Fairweather fault zone (Table S1) and analyzed in LaDiCaoz 2.1 (Zielke et al., 2015; Haddon et al., 2016). A. Base lidar map, elevation contours on 1-meter intervals. B. Offset analysis setup: topographic profiles (red and blue lines) and traced crest (red and blue dots) across the Fairweather fault zone (cyan line). Yellow dots mark bounds on red crest topography fit to blue crest topography. C. *In-situ* topographic profiles; red dots represent moraine crest cross-section selected (within yellow dots) for cross-correlation to crest along blue topographic profile, across the fault. D. Topographic profiles restored via cross-correlation: red crest cross-section back-slipped 43 meters to blue crest cross-section across fault. Vertical shift raises downstream elevations 12 m and may not be tectonic. E. Misfit curve for cross-correlation of red and blue crest cross sections; minimal misfit value marked by dark gray vertical bar represents best horizontal offset value from cross-correlation, light gray bar delineates visually determined offset range. F. Minimum horizontal offset (38 m) visually determined from back-slipping. G. Maximum horizontal offset (47 m) visually determined from back-slipping.

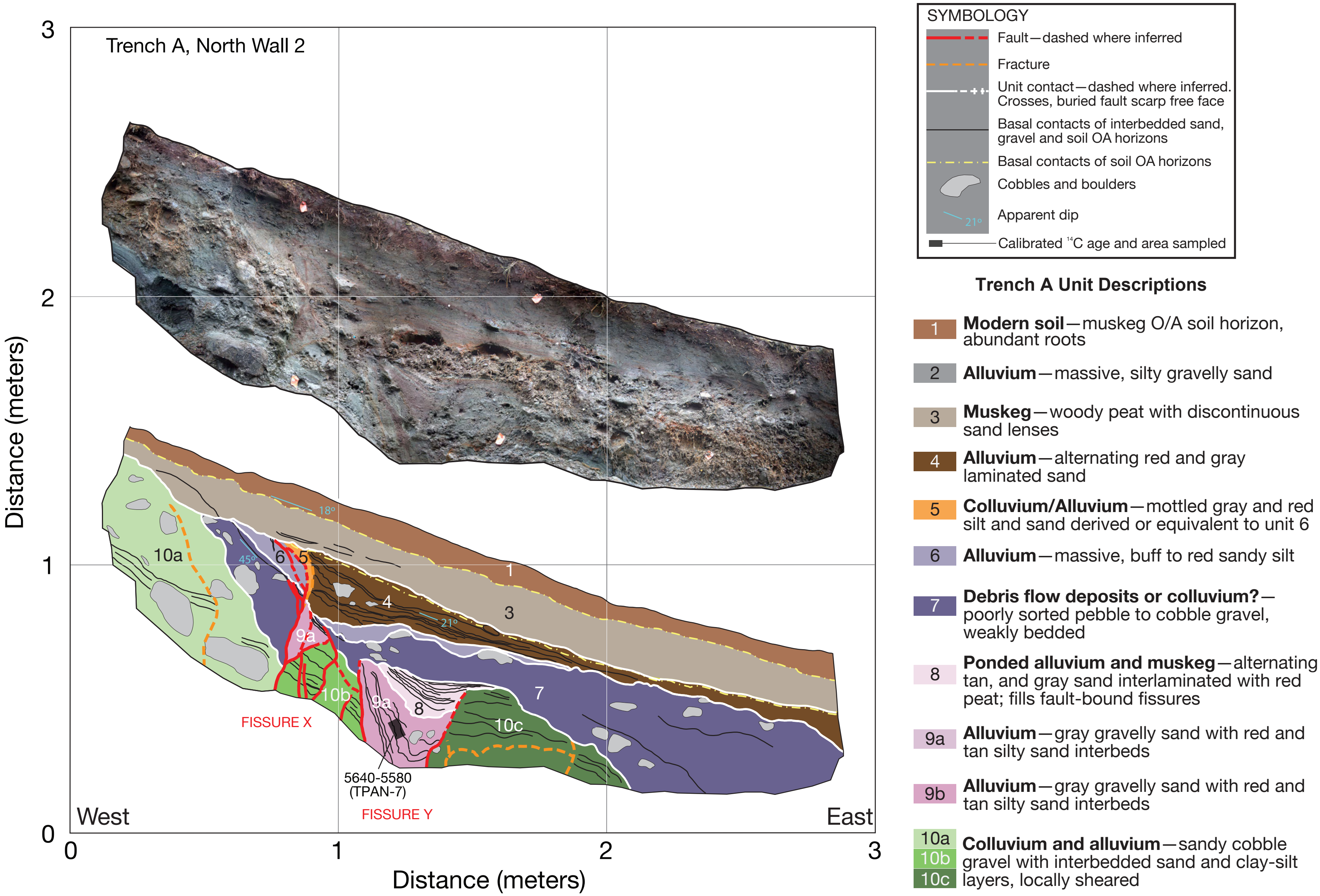

Figure S9. Uninterpreted photomosaic (upper) and stratigraphic and structural relationships logged (lower) of the second north wall exposure of trench A at the Tocher fan site along the Fairweather fault. This exposure was produced by excavating into the north wall, about 10 cm north of the exposure shown in Figure 11. Dark gray areas mark locations of detrital organic samples submitted for radiocarbon dating. Calibrated age ranges (95% confidence intervals) are shown in calendar years before CE 1950.

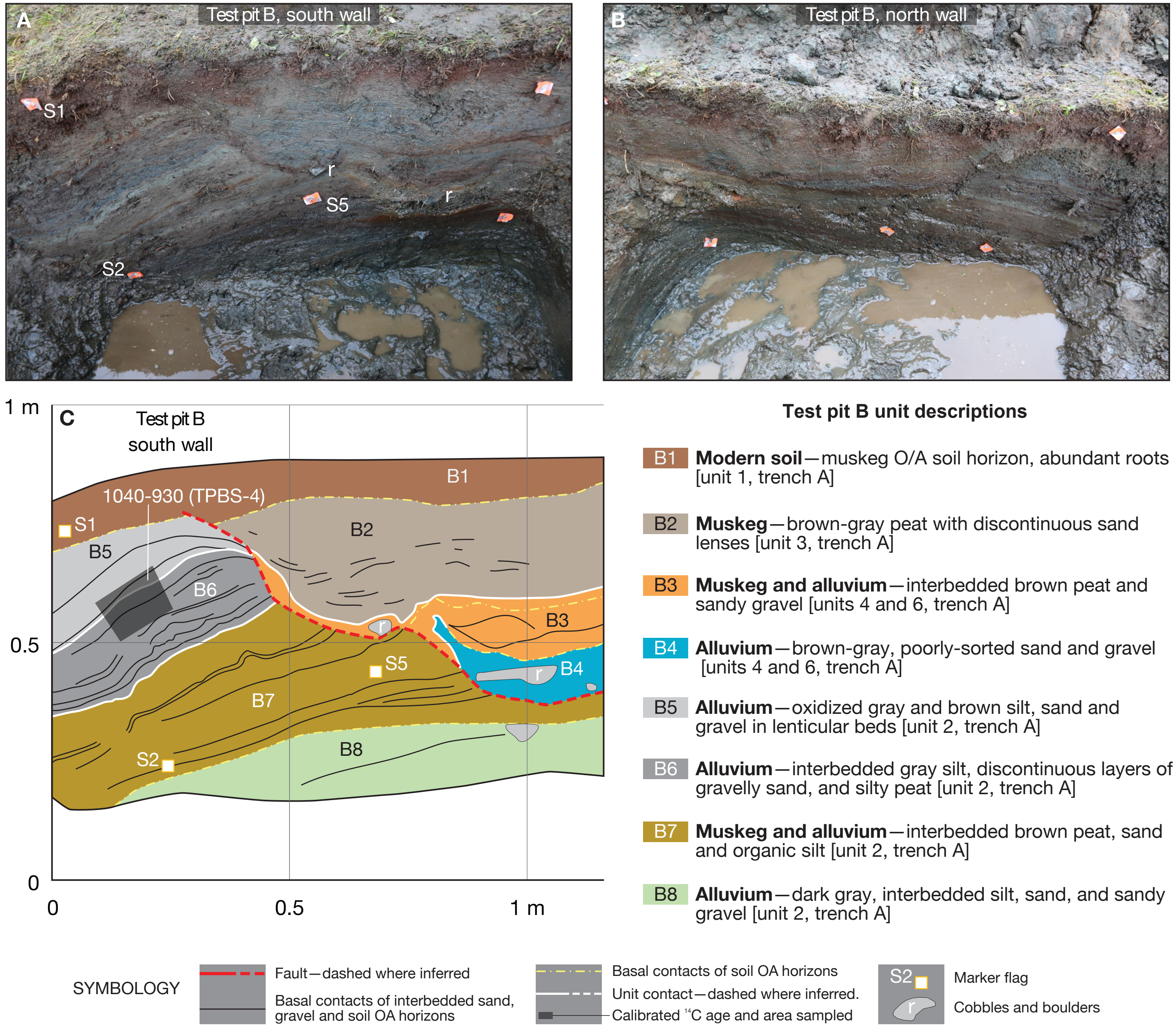

Figure S10. Uninterpreted photographs of the south (A) and north (B) walls of test pit B at the Tocher fan site along the Fairweather Fault. (C) Stratigraphic and structural relations logged in the south (A) wall of test pit B. Dark grey area marks the location of detrital organic material submitted for radiocarbon dating. Calibrated age ranges (95% confidence intervals) are shown in calendar years before CE 1950. Descriptions of stratigraphic units in test pit B are shown at lower right. Inferred correlative units in trench A, in brackets.

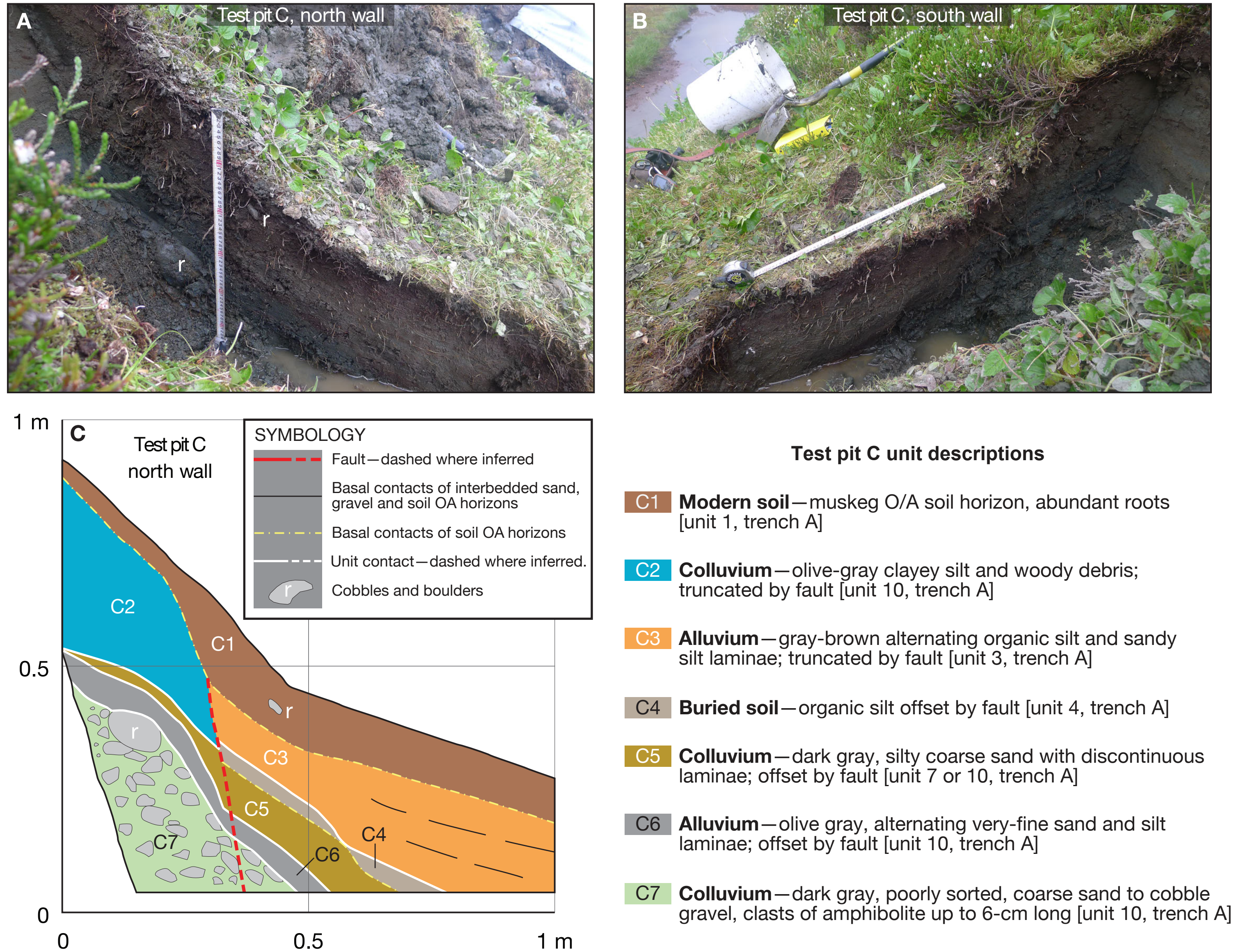

Figure S11. Uninterpreted photographs of the north (A) and south (B) walls of test pit C at the Tocher fan site along the Fairweather Fault. (C) Stratigraphic and structural relations logged in the north (A) wall of test pit C. Descriptions of stratigraphic units in test pit C are shown at lower right. Inferred correlative units in trench A, in brackets.

TABLE S1. RIGHT-LATERAL OFFSETS FROM LADICAOZ LIDAR ANALYSIS

Site	Latitude*	Longitude*	Horizontal offsets (m)†		Offset quality§	Description	Figure
			Preferred	Range			
Crillon Lake	58.590884	-137.376341	33	28–38	2	Central channel offset across well-defined primary Fairweather fault trace.	S3
Crillon Lake	58.590962	-137.377408	24	21–27	2	Central channel offset across well-defined secondary Fairweather fault trace.	S4
Finger Glacier	58.484596	-137.182235	112	105–116	2–3	Highest Finger Glacier moraine crest offset across Fairweather fault zone.	S7
Finger Glacier	58.483665	-137.182059	43	38–47	2	Recessional Finger Glacier moraine crest offset across Fairweather fault zone, first reported by Plafker et al. (1978).	S8

*Coordinates centered on offset landform west of fault trace.

†Offsets estimated as described by Zielke et al. (2015) and Haddon et al. (2016): Preferred values represent topographic cross-correlation results, Ranges of values represent plausible landform reconstructions from back-slipping.

§Offset quality rating of Salisbury et al. (2015) based on obliquity of landform intersection with fault trace, and fault zone width; ratings 1–3 correspond to best to worst quality, respectively.

Table S2. OxCal Sequence model results and code for radiocarbon age estimates of the South Crillon Glacier moraine.

Name	Unmodelled (BP)						Modelled (BP)					
	from	to	%	mu	sigma	median	from	to	%	mu	sigma	median
Sequence South Crillon Glacier chronology												
Boundary Start							11607	5131	95.4	7452	1818	6867
R_Date W-3311	6175	5050	95.3	5611	246	5619	6102	4980	95.4	5575	249	5588
R_Date W-3305	4797	3345	95.4	3960	332	3945	4797	3346	95.4	3960	332	3945
R_Date W-3313	1272	557	95.4	899	182	884	1294	565	95.4	940	183	927
Crillon moraine							999	98	95.4	521	265	500
Boundary End LIA 1850	101	100	95.4	101	0	101	101	100	95.4	101	0	101

OxCal code:

```
Plot(Crillon fan chronology)
{
 Sequence("South Crillon Glacier chronology")
 {
  Boundary("Start");
  Phase("SC1")
  {
   R_Date("W-3311", 4880, 200);
   R_Date("W-3305", 3600, 250);
  };
  R_Date("W-3313", 940, 200);
  Date("Crillon moraine");
  Boundary("End LIA", 1850);
 };
};
```

Table S3. OxCal Sequence model results and code for radiocarbon age estimates of Finger Glacier moraines offset by the Fairweather Fault.

Name	Unmodelled (BP)						Modelled (BP)					
	from	to	%	mu	sigma	median	from	to	%	mu	sigma	median
Sequence Finger Glacier moraine chronology												
Boundary Old neoglacial forest							12518	8420	95.4	9983	1233	9660
R_Date W-3306	9886	8385	95.3	9089	366	9087	9614	8335	95.4	8957	342	8934
Phase Old neoglacial advance												
R_Date W-3323	8510	7567	95.4	8015	238	8007	8453	7567	95.4	8010	233	8004
R_Date W-3322	8378	7487	95.4	7916	232	7904	8374	7489	95.4	7914	229	7902
R_Date W-3312	7156	5930	95.4	6504	289	6495	7156	5931	95.5	6505	290	6495
R_Date W-3310	4568	3480	95.4	4037	272	4027	4799	3689	95.4	4170	246	4161
R_Date W-3303	4784	3257	95.4	3935	332	3919	4356	3352	95.4	3823	252	3822
Highest FG moraine							4078	1614	95.4	2979	662	3078
Boundary Forest time							3531	1019	95.4	2134	710	2014
R_Date W-3307	1692	797	95.4	1237	205	1232	1703	830	95.4	1261	206	1255
Boundary Most recent advance time							1400	102	95.4	802	370	824
Boundary End LIA 1850	101	100	95.4	101	0	101	101	100	95.4	101	0	101

OxCal code:

```
 Plot(Finger_Glacier_Moraine_chronology)
 {
  Sequence("Finger Glacier moraine chronology")
  {
   Boundary("Old neoglacial forest");
   //Minimum age of oldest forest buried by neoglacial advance (Plafker et al., 1978)
   R_Date("W-3306", 8160, 300);
   //Maximum age for older neoglacial advance of Finger Glacier
   Phase("Old neoglacial advance")
   {
    R_Date("W-3323", 7170, 250);
```

```
   R_Date("W-3322", 7060, 250);
   R_Date("W-3312", 5670, 250);
  };
  //Minimum age of forest buried by intermediate neoglacial advance
  R_Date("W-3310", 3670, 200);
  //Maximum age of intermediate neoglacial advance of Finger Glacier
  R_Date("W-3303", 3580, 250);
  Date("Highest FG moraine");
  Boundary("Forest time");
  //Maximum age of most recent advance of Finger Glacier
  R_Date("W-3307", 1320, 200);
  Boundary("Most recent advance time");
  Boundary("End LIA", 1850);
 };
};
```

Table S4. OxCal Sequence model results and code for radiocarbon age estimates of surface fault rupture evident in Tocher fan Trench A.

Name	Unmodelled (BP)						Modelled (BP)					
	from	to	%	mu	sigma	median	from	to	%	mu	sigma	median
Sequence trench A chronology												
Boundary Start							8178	5585	95.4	6380	835	6108
R_Date TPAN-7	5644	5584	95.4	5600	19	5598	5644	5583	95.4	5600	18	5598
Event A3							5587	4848	95.4	5214	224	5214
Phase Unit 8 time												
R_Date TPAS-1	4828	4624	95.4	4720	59	4719	4828	4623	95.4	4720	59	4719
R_Date TPAS-5	4855	4726	95.4	4826	33	4835	4855	4725	95.4	4825	34	4835
Phase Unit 6 time												
R_Date TPAS-2	4521	4416	95.4	4470	33	4477	4521	4416	95.4	4470	33	4477
R_Date TPAS-6	899	735	95.4	788	43	778	900	735	95.4	794	46	780
Event A2							810	481	95.4	641	93	639
R_Date TPAS-3	510	464	95.4	489	22	493	510	464	95.4	489	20	493
Event A1							468	-5	95.4	241	144	240
Boundary End 1958	-7	-8	95.4	-7	0	-7	-7	-8	95.4	-7	0	-7

OxCal code:

```
Plot(Trench A earthquake chronology)
 {
  Sequence(Trench A chronology)
  {
   Boundary("Start");
   R_Date("TPAN-7", 4860, 20);
   Date("Event A3");
   Phase("Unit 8 time")
   {
    R_Date("TPAS-1", 4170, 20);
    R_Date("TPAS-5", 4240, 20);
   };
   Phase("Unit 6 time")
```

```
  {
   R_Date("TPAS-2", 3990, 25);
   R_Date("TPAS-6", 880, 15);
  };
  Date("Event A2");
  R_Date("TPAS-3", 410, 15);
  Date("Event A1");
  Boundary("End", 1958);
 };
};
```

Table S5. OxCal Sequence model results and code for radiocarbon age estimates of surface disturbances evident in Tocher fan Trench D.

Name	Unmodelled (BP)						Modelled (BP)					
	from	to	%	mu	sigma	median	from	to	%	mu	sigma	median
Sequence Trench D chronology												
Boundary Start							4409	3045	95.4	3496	425	3361
Phase Pre event D4												
R_Date TPDS-1	3171	3061	95.4	3112	32	3113	3170	3040	95.4	3109	32	3110
R_Date TPDS-8	1777	1620	95.5	1685	40	1698	1778	1620	95.4	1686	39	1698
R_Date TPDS-2	1695	1557	95.4	1618	41	1609	1695	1558	95.4	1622	41	1612
Event D4							1626	1207	95.4	1419	118	1419
Phase Between D4–D3												
R_Date TPDS-5	1281	1176	95.4	1223	33	1227	1283	1174	95.4	1220	35	1223
R_Date TPDS-3	893	734	95.4	778	35	772	893	735	95.4	779	36	773
R_Date TPDS-4	899	735	95.4	788	43	778	900	735	95.4	789	43	779
Event D3							763	527	95.4	646	70	645
R_Date TPDS-10	540	512	95.4	526	7	527	541	512	95.4	526	7	526
Events D1 and D2							513	-4	95.4	259	154	259
Boundary End	-7	-8	95.4	-7	0	-7	-7	-8	95.4	-7	0	-7
1958												

OxCal code:

```
Plot(Trench D event chronology)
 {
  Sequence("Trench D chronology")
  {
   Boundary("Start");
   Phase("Pre event D4")
   {
    R_Date("TPDS-1", 2950, 15);
    R_Date("TPDS-8", 1780, 15);
    R_Date("TPDS-2", 1710, 20);
```

```
  };
  Date("Event D4");
  Phase("Between D4–D3")
  {
   R_Date("TPDS-5", 1270, 25);
   R_Date("TPDS-3", 875, 15);
   R_Date("TPDS-4", 880, 15);
  };
  Date("Event D3");
  R_Date("TPDS-10", 505, 15);
  Date("Events D1 and D2");
  Boundary("End", 1958);
 };
};
```